CHEMISTRY OF MATERIALS

pubs.acs.org/cm

Article

Extending the Family of Hybrid Layered Fluoride Perovskites

Teng Li, Alasdair J. Bradford, Stephen L. Lee, and Philip Lightfoot*

Cite This: https://doi.org/10.1021/acs.chemmater.4c00633

Read Online

ACCESS | Metrics & More | Article Recommendations | Supporting Information

ABSTRACT: The family of hybrid layered fluoride perovskites has been extended, based on the only previously reported example $(enH_2)MnF_4$ (*en* = 1,2-diaminoethane), to include further divalent transition metals and longer chain diamines. The compounds $(enH_2)BF_4$, (*B* = Co, Ni) and $(bnH_2)BF_4$, (*bn* = 1,4-diaminobutane, *B* = Mn, Co) adopt the same space group ($P2_1/c$) as $(enH_2)MnF_4$, whereas $(pnH_2)BF_4$, (*pn* = 1,3-diaminopropane, *B* = Mn, Co) adopt the space group *Pnma*. Key differences in these structure types are shown to depend on the parity of the number of carbon atoms in the linear amine, which may be considered a structure-directing agent. Magnetic measurements on selected samples indicate differences in magnetic order that can be understood in terms of both the transition metal and the molecular species. All samples exhibit antiferromagnetic correlations but can in some cases develop a canted spin ferromagnetic component due to anisotropic exchange interactions. An additional compound, $(bn)Ni_2F_4$, has also been isolated, which exhibits a unique layered structure with *bn* acting as a ligand rather than in cationic form.

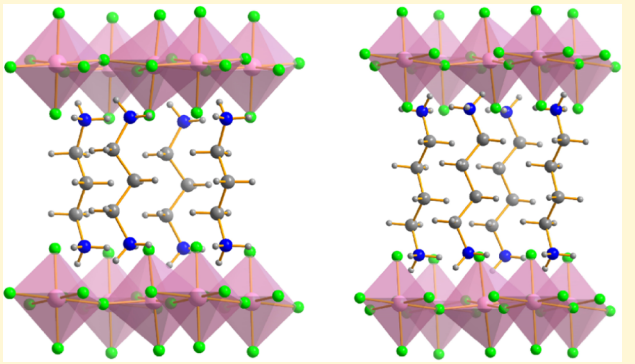

INTRODUCTION

Hybrid organic−inorganic fluorides are a diverse family of materials, encompassing many combinations of inorganic and organic cations and a wide range of structure types of differing dimensionalities.[1−3] However, in contrast to the enormous and diverse family of hybrid layered halide perovskite structures based on the heavier halides (Cl, Br, I),[4−6] there is, remarkably, only one previous report of an analogous hybrid fluoride perovskite, viz. $(enH_2)MnF_4$ (*en* = 1,2-diaminoethane).[7] Hybrid lead-fluoride perovskites, in particular, are unlikely to be formable from solution, first due to the high stability of PbF_2 but more importantly due to the relative size mismatch of Pb^{2+} and F^-. Lead-fluoride systems are therefore not a viable target for discovering new hybrid perovskites. Indeed, there are no examples of hybrid compounds containing only Pb-to-F bonds in the Cambridge Crystallographic Database. The "octahedral factor," μ, which is used as a guide to formability of perovskites, relies on the ionic radius ratio, i.e., $\mu = r(B^{n+})/r(X^{m-}) > 0.41$ for the formation of a stable BX_6 octahedral unit.[8,9] This is simply based on the concepts of close-packing of hard, spherical ions, a concept that is reasonably valid in the case of a hard anion, F^-, which also suggests that octahedral coordination will become unstable for $\mu > 0.73$. In fact, the detailed study of Li et al.[8] suggests perovskite stability in the range $0.442 < \mu < 0.895$. Using Shannon ionic radii,[10] for Pb^{2+} (1.19 Å), high-spin Mn^{2+} (0.83 Å), Co^{2+} (0.745 Å), Ni^{2+} (0.69 Å), and F^-(1.285 Å), the corresponding μ factors for BF_6 octahedra are 0.93, 0.65, 0.58, 0.54 for *B* = Pb, Mn, Co, Ni, respectively. Therefore, a more natural choice in the search for hybrid layered fluoride perovskites might target divalent transition metals; indeed, there are many examples of perovskite-related all-inorganic transition metal fluorides, both layered (ABF_4, A_2BF_4)[11] and three-dimensional (ABF_3).[9] Moreover, there are recent examples of hybrid layered fluorides containing octahedral transition metal cations, with structures related to but distinct from perovskite.[12] In terms of physical properties, there are also expected to be significant differences between hybrid transition metal fluorides and lead halides, for example. The much more ionic nature of the *B*−F bond versus Pb−*X* is likely to preclude useful semiconducting behavior in the former. In contrast, transition metals obviously lend themselves toward magnetic properties, and it is also well-established that electrical polarity can be "designed-in" in inorganic layered perovskites[13]—an option which is greatly enhanced by incorporating asymmetric, molecular species at the interlayer sites.[6,14] Multiferroic materials may also be a future target for a family of hybrid layered fluoride perovskites.

The purpose of the present paper is to expand our earlier discovery of $(enH_2)MnF_4$ to demonstrate that such systems are likely to give rise to a much wider family of potentially useful

Received: March 4, 2024
Revised: April 27, 2024
Accepted: April 30, 2024

Table 1. Crystal Structure Refinement Data for Compounds 1, 2, 5, and 6

temperature	1 (173 K)	2 (173 K)	2 (298 K)	5 (173 K)	5 (298 K)	6 (173 K)	6 (298 K)
formula	$(C_2H_{10}N_2)CoF_4$	$(C_2H_{10}N_2)NiF_4$	$(C_2H_{10}N_2)NiF_4$	$(C_4H_{14}N_2)MnF_4$	$(C_4H_{14}N_2)MnF_4$	$(C_4H_{14}N_2)CoF_4$	$(C_4H_{14}N_2)CoF_4$
formula weight	197.05	196.81	196.81	221.11	221.11	225.10	225.10
color/habit	purple/chip	green/chip	green/chip	colorless/chip	colorless/chip	purple/chip	purple/chip
crystal size (mm^3)	0.20 × 0.16 × 0.06	0.05 × 0.05 × 0.03	0.05 × 0.05 × 0.03	0.22 × 0.14 × 0.03	0.22 × 0.14 × 0.03	0.12 × 0.10 × 0.03	0.12 × 0.10 × 0.03
crystal system	monoclinic	monoclinic	monoclinic	monoclinic	monoclinic	monoclinic	monoclinic
Sspace group	$P2_1/c$	$P2_1/c$	$P2_1/c$	$P2_1/c$	$P2_1/c$	$P2_1/c$	$P2_1/c$
a (Å)	8.0384(5)	8.0461(8)	8.0449(8)	10.6452(8)	10.6445(8)	10.5061(7)	10.5009(7)
b (Å)	5.8987(4)	5.8058(5)	5.8218(6)	6.0329(4)	6.0475(4)	5.9399(4)	5.9562(4)
c (Å)	5.8754(4)	5.7911(6)	5.7995(6)	5.9929(4)	6.0113(4)	5.9078(4)	5.9284(4)
β (deg)	90.703(12)	90.298(14)	90.336(16)	91.422(6)	91.498(6)	92.251(9)	92.375(9)
V ($Å^3$)	278.57(3)	270.52(5)	271.62(5)	384.75(5)	386.83(5)	368.39(4)	370.48(4)
Z	2	2	2	2	2	2	2
ρ_{calc} (g/cm^3)	2.349	2.416	2.407	1.909	1.898	2.029	2.018
μ (mm^{-1})	3.076	3.582	3.567	1.726	1.716	2.340	2.327
$F(000)$	198.0	200.0	200.0	226.0	226.0	230.0	230.0
reflns collected	2288	2307	2312	3063	3086	3568	2883
independent reflns	475	479	480	671	673	638	633
	[R(int) = 0.046]	[R(int) = 0.106]	[R(int) = 0.155]	[R(int) = 0.053]	[R(int) = 0.046]	[R(int) = 0.109]	[R(int) = 0.092]
goodness of Fit	1.036	1.029	0.956	1.223	1.168	1.022	1.008
final R indices ($I > 2\sigma(I)$)	$R1$ = 0.0434	$R1$ = 0.0480	$R1$ = 0.0491	$R1$ = 0.0327	$R1$ = 0.0303	$R1$ = 0.0590	$R1$ = 0.0630
	$wR2$ = 0.1281	$wR2$ = 0.1030	$wR2$ = 0.1029	$wR2$ = 0.0935	$wR2$ = 0.0867	$wR2$ = 0.1472	$wR2$ = 0.1457
largest diff. peak/hole (e $Å^{-3}$)	1.378/−0.540	0.634/−0.705	0.677/−0.569	0.765/−0.359	0.692/−0.285	1.348/−1.119	1.306/−0.885

Table 2. Selected Bond Lengths (Å) and Bond Angles (deg) for Compounds 1, 2, 5, and 6

	1 (173 K)	2 (173 K)	2 (298 K)	5 (173 K)	5 (298 K)	6 (173 K)	6 (298 K)
M−F2	2.003(3)	1.973(4)	1.972(4)	2.0939(19)	2.0964(18)	1.990(3)	1.988(4)
M−F1	2.093(2)	2.057(6)	2.056(7)	2.1549(17)	2.1584(16)	2.102(4)	2.107(4)
M−F1	2.106(2)	2.065(6)	2.072(6)	2.1553(17)	2.1603(16)	2.117(4)	2.122(4)
M−F−M	4.1628(2)	4.1001(3)	4.1088(3)	4.2518(2)	4.2634(2)	4.1888(2)	4.2019(2)
M−F−M angle	165.00(16)	168.3(3)	168.9(3)	161.12(10)	161.64(10)	166.27(19)	166.85(19)
N1−(H)---F1	2.759(7)	2.788(10)	2.804(12)	2.777(4)	2.789(3)	2.786(6)	2.804(7)
N1−(H)···F2	2.702(5)	2.713(8)	2.718(9)	2.687(3)	2.691(3)	2.711(6)	2.713(6)
N1−(H)···F2	2.753(11)	2.77(2)	2.75(2)	2.755(4)	2.768(3)	2.772(7)	2.780(7)
N1−H−F1 angle	176.3	174.4	175.3	174.9	175.1	173.3	173.3
N1−H−F2 angle	171.1	167.9	168.9	175.8	175.1	175.5	176.2
N1−H−F2 angle	158.0	160.7	160.7	156.6	157.2	155.8	155.1

materials. In particular, we demonstrate that other divalent transition metals and longer chain amines may be incorporated into layered perovskite systems of this family. The syntheses, crystal structures, and preliminary magnetic properties of seven new compounds, $(enH_2)BF_4$ (B = Co, Ni), $(pnH_2)BF_4$ (pn = 1,3-diaminopropane, B = Mn, Co), $(bnH_2)BF_4$ (bn = 1,4-diaminobutane, B = Mn, Co), and $(bn)Ni_2F_4$ are reported.

EXPERIMENTAL SECTION

Chemicals and Materials. Cobalt(II) fluoride (CoF_2, 98%), manganese(II) fluoride (MnF_2, 99%), nickel(II) fluoride (NiF_2, 97%), ethylene glycol ($(CH_2OH)_2$, 99%), and hydrofluoric acid (HF, 48−51% wt. in water) were purchased from Alfa Aesar. 1,2-diaminoethane ($C_2H_8N_2$, ≥99%), 1,3-diaminopropane ($C_3H_{10}N_2$, ≥99%), and 1,4-butanediamine ($C_4H_{12}N_2$, ≥99%) were purchased from Sigma-Aldrich. All chemicals were used as-received without any further purification.

Synthesis. Single crystals of compounds **1**−**7** were prepared by hydro/solvothermal methods. Specific reaction conditions are listed in Supporting Information. In detail, fluoride salts in certain molar ratios were weighed, followed by the addition of solutions. Hydrofluoric acid was slowly added into the solutions with magnetic stirring. Then, the mixtures were transferred to Teflon-lined stainless-steel autoclaves. The autoclaves were then sealed and put into ovens at the stated temperature for several days. After reaction, the autoclaves were cooled naturally in the oven to room temperature. Products were taken out, filtered with distilled water and ethanol, and dried overnight in an oven at 90 °C.

CHARACTERIZATION

Single Crystal X-Ray Diffraction. Single crystal X-ray diffraction data were collected on a Rigaku SCX Mini diffractometer at 173 and 298 K using Mo−K_α radiation (λ = 0.71075 Å). Data were collected using CrystalClear (Rigaku) software.[15] Structures were solved by direct methods using SHELXT,[16] and full-matrix least-squares refinements on F^2 were carried out using SHELXL-2018/3 incorporated in the WinGX program.[17] Absorption corrections were performed empirically from equivalent reflections based on multiscans by using CrystalClear. Non-H atoms were refined anisotropically, and hydrogens were treated as riding atoms.

Powder X-Ray Diffraction (PXRD). The crystalline samples were ground for 30 min into a proper powder and loaded into steel discs. PXRD data were collected between 3 and 70° for 1 h at room temperature on a Panalytical Empyrean diffractometer, using $CuK_{\alpha1}$ radiation. Rietveld refinements were carried out using the GSAS package and the

https://doi.org/10.1021/acs.chemmater.4c00633
Chem. Mater. XXXX, XXX, XXX−XXX

EXPGUI interface.[18] Fixed crystallographic models were used, based on CIF files from the single crystal refinements at 298 K, with only profiles and lattice parameters being refined.

Magnetism. The magnetic measurements were carried out on a Quantum Design (MPMS XL) SQUID magnetometer. Data were collected by cooling a known mass of material at a 100 Oe field between 300 and 2 K. Measurements of magnetization versus applied field were carried out between −5000 and 5000 Oe at different temperatures.

RESULTS AND DISCUSSION

Crystal Structures of $(enH_2)BF_4$ (B = Co (1), Ni (2)). From single crystal XRD at 173 K, both **1** and **2** are found to be isostructural with our previous compound $(enH_2)MnF_4$. In our earlier work,[7] we also collected single crystal XRD data at 93 and 298 K; no structural phase transitions were found. In the present cases, we only collected an additional data set for **1** at 298 K, which also revealed the same structure as that at 173 K. Parameters of the single crystal studies at 173 K are reported in Table 1, with selected bond distances and angles in Table 2. The crystal structure of **1** and **2** is presented in Figure 1. These compounds adopt the monoclinic crystal system, space group $P2_1/c$, with only a small reduction of unit cell volume as a consequence of the changes in the B^{2+} ionic radius. The structure may be regarded as derived from the aristotype Dion−Jacobson (DJ)-type layered perovskite ($TlAlF_4$ structure), with single corner-sharing octahedral layers, $[BF_4]_\infty$, in the bc plane, separated by the $(enH_2)^{2+}$ cations along the a-axis. Adjacent octahedral layers occur in near-eclipsed configuration relative to each other. However, it should be noted that the degree of "layer shift" is a variable parameter, and in this case, its small value is reflected in the slight deviation of the β angle away from 90°. This structure type is the most common among the lead halide analogues[6] and has the Glazer-like tilt system a^-a^-c. The $(enH_2)^{2+}$ moieties adopt a "fully stretched" conformation, with the N−C−C−N torsion angles close to 180°. Strong H bonds occur between these moieties and the F atoms of the inorganic layers (Table 2).

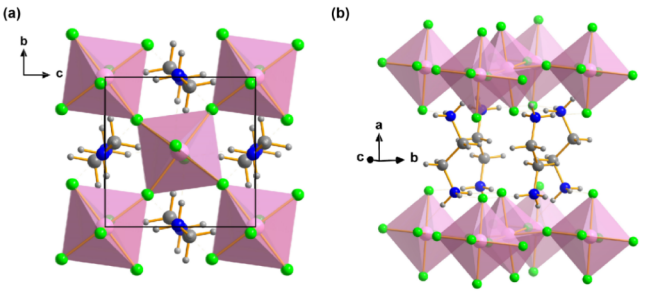

Figure 1. Crystal structure of **1** and **2** (a) along a and (b) perpendicular to a.

Crystal Structures of $(pnH_2)BF_4$ (B = Mn (3), Co (4)). Single crystal XRD data for both **3** and **4** were collected at both 173 and 298 K. Again, no evidence for a structural phase transition was found within this region. Table 3 includes the crystallographic parameters at 173 K, and Table 4 includes the corresponding bond lengths and angles. It can be seen that **3** and **4** are isostructural, but the structure type differs from that of **1** and **2**. Although the basic DJ-type structure is retained (Figure 2), the space groups and unit cell metrics are significantly different. The orthorhombic space group this time necessitates perfect eclipsing of neighboring octahedral layers, whereas the effectively "doubled" b-axis is caused by differing behavior of these neighboring layers. The key difference lies in the relative out-of-plane tilting of adjacent layers along the b-axis. These can be seen to alternate in opposite senses,"up−down," leading to the tilt system being best described as $a^-a^-c/-(a^-a^-)c$. Perhaps surprisingly, this specific structure type, i.e., one which incorporates both out-of-plane tilting, and rotations of octahedra around an axis perpendicular to the layer direction, but does not allow

Table 3. Crystal Structure Refinement Data for Compounds 3, 4, and 7

temperature	3 (173 K)	3 (298 K)	4 (173 K)	4 (298 K)	7 (173 K)	7 (298 K)
Formula	$(C_3H_{12}N_2)MnF_4$	$(C_3H_{12}N_2)MnF_4$	$(C_3H_{12}N_2)CoF_4$	$(C_3H_{12}N_2)CoF_4$	$(C_4H_{12}N_2)Ni_2F_4$	$(C_4H_{12}N_2)Ni_2F_4$
formula weight	207.09	207.09	211.08	211.08	140.77	140.77
color/habit	colorless/chip	colorless/chip	purple/chip	purple/chip	green/chip	green/chip
crystal size (mm^3)	0.13 × 0.10 × 0.02	0.17 × 0.11 × 0.04	0.09 × 0.04 × 0.03	0.09 × 0.04 × 0.03	0.25 × 0.06 × 0.02	0.25 × 0.06 × 0.02
crystal system	orthorhombic	orthorhombic	orthorhombic	orthorhombic	monoclinic	monoclinic
space group	*Pnma*	*Pnma*	*Pnma*	*Pnma*	$P2_1/c$	$P2_1/c$
a (Å)	6.0080(4)	6.0083(5)	5.9215(4)	5.9384(4)	10.6818(7)	10.6838(8)
b (Å)	18.7802(13)	18.7807(17)	18.6127(14)	18.5971(15)	5.1371(3)	5.1409(4)
c (Å)	6.0349(4)	6.0502(5)	5.9258(4)	5.9430(5)	7.4334(5)	7.4586(5)
β (deg)	90	90	90	90	94.379(8)	94.505(8)
V ($Å^3$)	680.93(8)	682.71(10)	653.11(8)	656.33(9)	406.71(5)	408.39(5)
Z	4	4	4	4	4	4
ρ_{calc} (g/cm^3)	2.020	2.015	2.147	2.136	2.299	2.289
μ (mm^{-1})	1.943	1.938	2.632	2.619	4.641	4.622
$F(000)$	420.0	420.0	428.0	428.0	284.0	284.0
reflns collected	4627	4845	6032	4444	3231	3248
independent reflns	614	621	638	587	507	566
	[R(int) = 0.158]	[R(int) = 0.099]	[R(int) = 0.072]	[R(int) = 0.058]	[R(int) = 0.080]	[R(int) = 0.036]
goodness of fit	0.972	1.064	1.004	1.046	0.897	1.017
final R indices ($I > 2\sigma(I)$)	$R1$ = 0.0388	$R1$ = 0.0317	$R1$ = 0.0324	$R1$ = 0.0328	$R1$ = 0.0293	$R1$ = 0.0212
	$wR2$ = 0.0819	$wR2$ = 0.0656	$wR2$ = 0.0715	$wR2$ = 0.0804	$wR2$ = 0.0654	$wR2$ = 0.0538
largest diff. peak/hole (e $Å^{-3}$)	0.455/−0.420	0.335/−0.321	0.372/−0.518	0.394/−0.439	0.620/−0.717	0.374/−0.340

https://doi.org/10.1021/acs.chemmater.4c00633
Chem. Mater. XXXX, XXX, XXX−XXX

Table 4. Selected Bond Lengths (Å) and Bond Angle (deg) Ranges for Compounds 3 and 4

	3 (173 K)	3 (298 K)	4 (173 K)	4 (298 K)
M−F2	2.003(3)	1.973(4)	2.0939(19)	2.0964(18)
M−F1	2.093(2)	2.057(6)	2.1549(17)	2.1584(16)
M−F1	2.106(2)	2.065(6)	2.1553(17)	2.1603(16)
M−F−M	4.1628(2)	4.1001(3)	4.2518(2)	4.2634(2)
M−F−M angle	165.00(16)	168.3(3)	161.12(10)	161.64(10)
N1−(H)···F1	2.759(7)	2.788(10)	2.777(4)	2.789(3)
N1−(H)···F2	2.702(5)	2.713(8)	2.687(3)	2.691(3)
N1−(H)···F2	2.753(11)	2.77(2)	2.755(4)	2.768(3)
N1−H−F1 angle	176.3	174.4	174.9	175.1
N1−H−F2 angle	171.1	167.9	175.8	175.1
N1−H−F2 angle	158.0	160.7	156.6	157.2

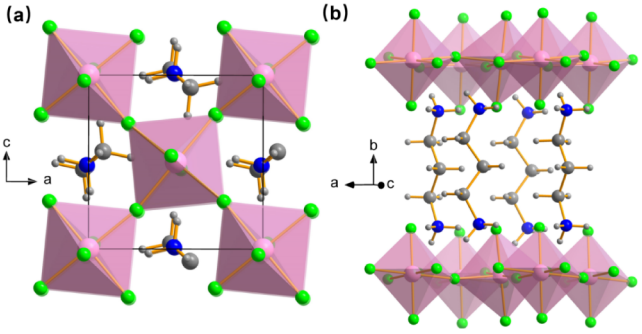

Figure 2. Crystal structure of **3** and **4** (a) along *b* and (b) perpendicular to *b*.

deviation from ideal DJ-type eclipsed layers, has not been seen in hybrid lead halides (see Table 2 in ref. 6for related but distinct structural variants). However, it has been seen in transition metal chloride analogues, for example, (pnH_2)-$MnCl_4$[19] and some copper chlorides.[20] In the present structures, the amine moieties again adopt a fully stretched conformation.

Crystal Structures of $(bnH_2)BF_4$ (*B* = Mn (5), Co (6)). Crystallographic details of **5** and **6** at 173 K are presented in Tables 1 and 2. The two compositions are again isostructural; moreover, the structural resemblance to **1** and **2** can be immediately seen in the unit cell metrics and space group, $P2_1/c$, the essential difference being an increase in the *a* parameter from ∼8.0 to ∼10.6 Å to accommodate the longer amine chain. Comparative views of the structures are shown in Figure 3. The configuration of the amine moiety is again all-*trans*. The octahedral tilt system is the same, a^-a^-c, and there is one octahedral layer per unit cell repeat (contrasting to two in **3** and **4**).

Hydrogen Bonding and Octahedral Tilting. Earlier work[19,21] has recognized the same "parity" effect in terms of the number of carbon atoms (C*n* = odd or even) in the amine chain dictating the tilt system in the analogous $(H_3N(CH_2)_nNH_3)BCl_4$ family. The difference can be ascribed to the differing symmetries of the amine moieties: for an all-*trans* configuration, the point groups are ideally 2/*m* (centrosymmetric) for *n* even and *mm*2 (polar) for *n* odd. This has corresponding consequences for the potential H-bonding interactions between the amines and fluoride ligands of the inorganic layers. Specifically, the inversion symmetry for *n* = 2

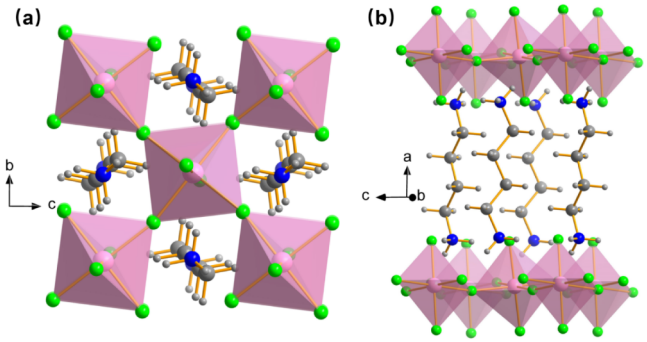

Figure 3. Crystal structure of **5** and **6** (a) along*a* and (b) perpendicular to *a*.

and *n* = 4 amines is imposed on the neighboring octahedral layers, whereas the *n* = 3 layers are directed toward mirror symmetry, leading to the alternating sense of tilting of adjacent layers. Figure 4 shows expanded details of these H-bonding

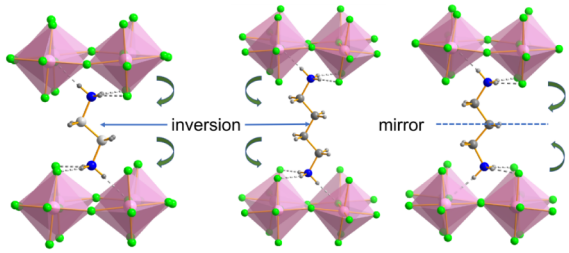

Figure 4. H-bonding interactions for **1** (*n* = 2), **6** (*n* = 4), and **4** (*n* = 3).

interactions for **1**, **4**, and **6**. In each case, there is one hydrogen bond from each atom of the $-NH_3$ group to a single F atom (assuming maximum H···F distances of 2.5 Å), resulting in two to apical Fs and one to the in-plane F.

Although no phase transitions are observed in the present family in the temperature ranges studied, these are common and well-studied in the analogous chlorides,[19] and it is likely that these may also occur in the present family at elevated temperatures, due to changes in conformation or disordering of the amine moieties, with consequent changes in octahedral tilting.

Crystal Structure of $(bn)Ni_2F_4$ (7). All of our attempts to prepare C3 or C4 analogues of the Ni-containing compound, **2**, were unsuccessful under similar experimental conditions. Instead, a novel and unique layered structure (**7**) was isolated in the case of the 1,4-diaminobutane. Crystallographic details are shown in Tables 3 and 5, and views of the structure are shown in Figure 5. Instead of containing corner-sharing octahedral layers, the structure displays both corner- and edge-sharing of Ni-centered octahedra. The single Ni coordination environment consists of five fluorine atoms and one nitrogen, i.e., the *bn* moiety in this case remains unprotonated and instead acts as a ligand to the Ni center. The amine retains a fully stretched configuration and forms direct covalent bridges between neighboring octahedral layers. The layers can be described as composed of chains of edge-sharing $NiNF_5$ octahedra running along the *b*-axis, where the edge-sharing connectivity alternates *cis*−*trans*. These chains are linked through shared vertices by identical chains (for clarity, the two sets of chains are shown in different colors in Figure 5). It is

https://doi.org/10.1021/acs.chemmater.4c00633
Chem. Mater. XXXX, XXX, XXX−XXX

Table 5. Selected Bond Lengths (Å) and Bond Angle (deg) Ranges for Compound 7

	7 (173 K)	7 (298 K)
Ni−F1	1.991(2)	1.9900(14)
Ni−F1	2.031(2)	2.0322(14)
Ni1−F2	2.039(2)	2.0428(14)
Ni1−F2	2.040(2)	2.0459(13)
Ni1−F2	2.076(2)	2.0810(14)
Ni1−N1	2.042(3)	2.047(2)
Ni−F−Ni	3.0321(8)	3.0347(5)
Ni−F−Ni angle	129.2(1)	129.28(7)
Ni−F−Ni angle	97.87(9)	96.50(6)
N1−(H)···F1	2.872(4)	2.857(3)
N1−(H)···F2	2.984(4)	2.988(3)
N1−H−F1 angle	159.5(2)	159.3(1)
N1−H−F2 angle	97.2(2)	97.3(1)
Ni1−F1−N1 angle	40.48(7)	40.56(5)
Ni1−F2−N1 angle	43.06(7)	43.12(5)

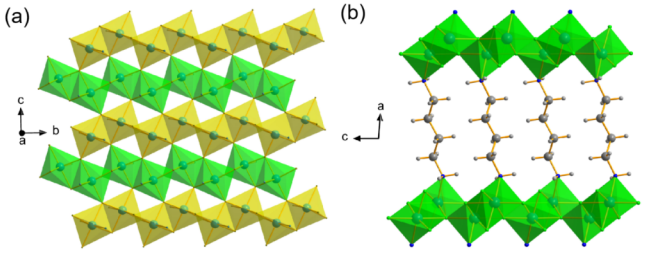

Figure 5. Crystal structure of **7** (a) in the *bc*-plane (the yellow and green colors represent different octahedral chains along the *b*-axis) and (b) perpendicular to the *a*-axis.

not clear from the reaction conditions why the *bn* should choose to act as a ligand in this case rather than a counterion.

We are unaware of any closely similar structures to **7** in metal fluoride chemistry, although Leblanc et al.[11] report that mixed edge/corner-sharing octahedral layers of differing connectivity do exist, for example, in the mixed metal fluoride $Ba_4Cu_2Al_3F_{21}$ and related compounds.

Magnetic Properties. The magnetic properties of **1**, **3**, **4**, and **5** have been investigated. It should be noted that samples of **3**, **4**, and **5** contain significant magnetic impurities (the fluorides MF_2), further details of which are provided in the following sections and in the Supporting Information. As discussed further below, there are some indications at low temperature of the presence of small amounts of paramagnetic impurities in the susceptibilities of both **3** and **5**, both of which exhibit low dimensional order. This is manifest as a flattening or small upturn in the susceptibility at low temperatures, which might possibly be attributed to a paramagnetic signal from nonordered phases. This cannot, however, arise from the known impurities MF_2, since both of the phases MnF_2 and CoF_2 are known to order antiferromagnetically at much higher temperature (T_N = 67.7 K and T_N = 39.1 K) respectively.[22] MnF_2 and CoF_2 would, therefore, only be expected to make a contribution to the measured signal while in the paramagnetic phase, admitting the possibility of small systematic errors in the determination of the moment values of samples **3**, **4**, and **5** from the high temperature susceptibility data.

Figure 6a depicts the χ versus T plot for **1** under an applied field of 100 Oe, which shows a slow increase within the region 100 < T < 300 K. A large discontinuous jump of the susceptibility ~80 K clearly indicates a magnetic phase transition with a ferromagnetic component. The inverse susceptibility plot was fitted with the Curie−Weiss law for T > 100 K (Figure 6b), leading to a Curie constant, C = 4.35 cm^3

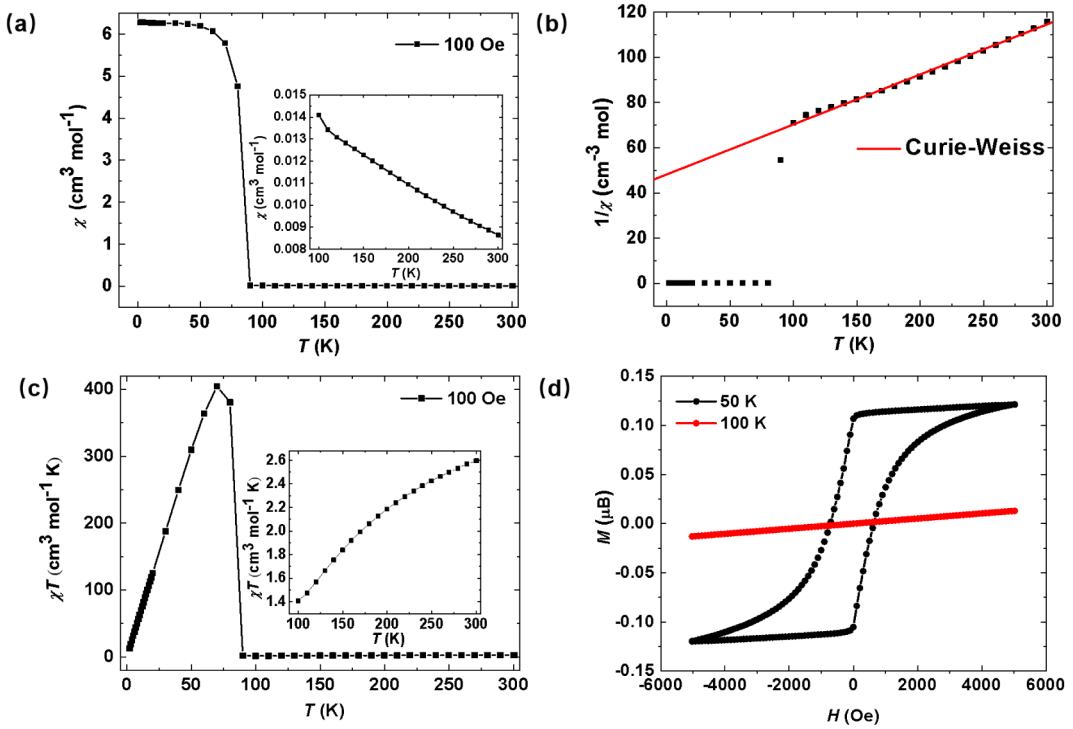

Figure 6. Magnetic data of **1**: (a) χ versus T (the inset shows the plot at high temperature). (b) $1/\chi$ versus T and the Curie−Weiss fit to $1/\chi$. (c) χT versus T (the inset shows the plot at high temperature). (d) Magnetization (M) versus magnetic field (H) at 100 K and hysteresis loop at 50 K.

https://doi.org/10.1021/acs.chemmater.4c00633
Chem. Mater. XXXX, XXX, XXX−XXX

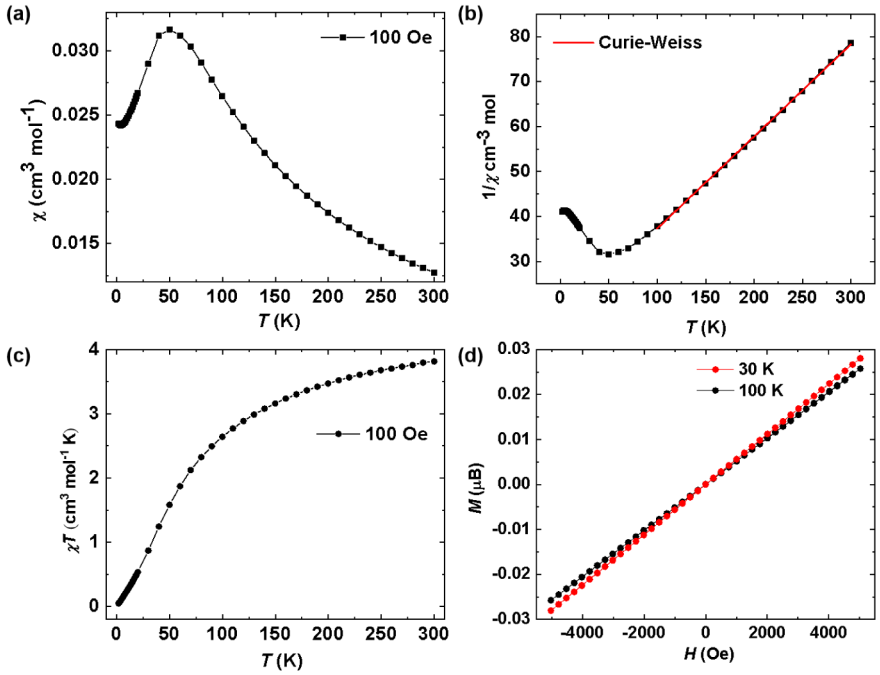

Figure 7. Magnetic data of **3**: (a) χ versus T at 100 Oe. (b) $1/\chi$ versus T and the Curie–Weiss fit to $1/\chi$ at 100 Oe. (c) χT versus T at 100 Oe. (d) Magnetization (M) versus magnetic field (H) at 30 K (red) and 100 K (black).

mol^{-1} K and the Weiss constant, $\theta = -199$ K, which indicates a strong overall antiferromagnetic interaction. The derived effective moment, $\mu_{eff} = 5.9\ \mu_B$, is significantly higher than the spin-only value (3.87 μ_B) due to a strong orbital contribution arising from the high-spin octahedral Co^{2+} (d^7, $^4T_{1g}$) configuration. Due to the high purity of this phase and the lack of any signatures of magnetic impurity, there is high confidence in the accuracy of this moment size.

At 300 K, χT is 2.60 cm^3 mol^{-1} K, which is lower than C, indicating a significant antiferromagnetic coupling between the Co^{2+} ions at room temperature. Upon cooling, χT monotonically decreases before arising abruptly at the transition around 80 K (Figure 6c). The continued decrease in χT below the transition just reflects the approach to saturation of the moment measured at a fixed field. The sign of the Weiss constant clearly indicates antiferromagnetic correlations above the transition $T_N \sim 80$ K, indicating that the ordered state has long-range antiferromagnetic order. However, the sharp spontaneous onset of a nonzero moment at low field strongly suggests a ferromagnetic component, which is further supported by the observation of strong magnetic hysteresis below T_N (Figure 6d). The hysteresis loop between ±5000 Oe shown in Figure 6d has some interesting features. The ferromagnetic component of the moment is relatively small compared to $\mu_{eff} = 5.9\ \mu_B$, suggesting a canting of the ordered antiferromagnetic moments along the field direction. This most likely arises from the influence of in-plane anisotropic Dzyaloshinskii–Moriya (DM) exchange interactions that are commonly observed in layered perovskite structures, where tilting of the octahedra occurs. In the absence of single crystal experiments, we cannot make a detailed analysis of the moment direction and additional sources of magnetic anisotropy. Nonetheless, both the shape of the hysteresis curve and the large magnetic coercivity are interesting. The shape is highly reminiscent of magnetic reversal of vortex-like structures, as observed, for example, in nanoscale magnetic systems.[23] This could indicate the presence of some kind of chiral or vortex domain structure in this material, which could arise from the interplay of different sources of magnetic anisotropy, including DM interactions. Further detailed measurements of single crystals are required to elucidate these observations.

The magnetic properties of **3** (with ~5.4% antiferromagnetic MnF_2 impurities, $T_N = 67$ K[24]) have also been investigated by SQUID magnetometry. The χ versus T plot at 100 Oe is depicted in Figure 7a. χ initially increases during cooling then exhibits a broad maximum around 50 K. The Curie constant, $C = 4.88$ cm^3 mol^{-1} K and Weiss constant, $\theta = -82.07$ K were deduced from the $1/\chi$ versus T plot for $T > 100$ K (Figure 7b), indicating an overall antiferromagnetic exchange interaction. The derived effective moment, $\mu_{eff} = 6.25\ \mu_B$ is similar to those of the corresponding Mn^{2+} compound $(enH_2)MnF_4$.[7] This is higher than the theoretical spin-only state and as with sample **1** indicates the presence of orbital contributions to the moment. The derived moment is significantly higher than that of the known impurity phase MnF_2 ($\mu_{eff} = 5.04\ \mu_B$), so the possible ca. 5% contribution of the latter is unlikely to explain the high value of the measured effective moment. The broad peak in $\chi(T)$ (Figure 7c) is characteristic of a 2D Heisenberg antiferromagnet, as might be expected from the negative Weiss constant coupled with the large separation of the perovskite layers, leading to very weak interlayer coupling. Once large area 2D antiferromagnetic correlations develop (on the low temperature side of the maximum in $\chi(T)$), any magnetic anisotropy will typically lead to the development of long-range three-dimensional order. This onset is frequently not accompanied by any clear signature in the bulk dc magnetization on powder samples, requiring microscopic measurements like neutron diffraction or muon-spin rotation to detect this. Signatures can be present in ac susceptibility or may also manifest as directional anisotropy in dc magnetization of single crystals. In the absence of such data, we can speculate

https://doi.org/10.1021/acs.chemmater.4c00633
Chem. Mater. XXXX, XXX, XXX−XXX

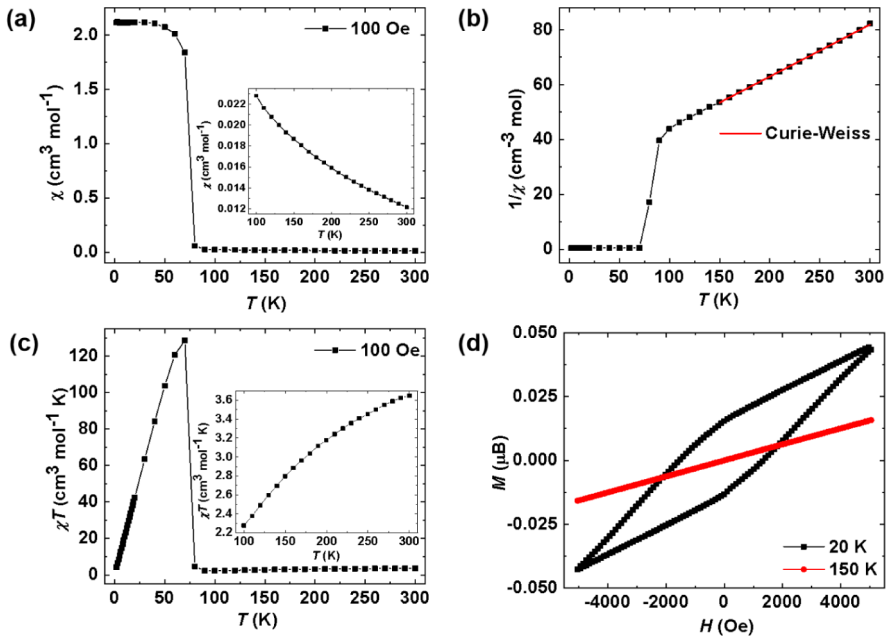

Figure 8. Magnetic data of **4**: (a) χ versus T at 100 Oe (the inset shows the plot at high temperature). (b) $1/\chi$ versus T and the Curie−Weiss fit to $1/\chi$. (c) χT versus T (the inset shows the plot at high temperature). (d) Magnetization (M) versus magnetic field (H) at 150 K and hysteresis loop at 20 K.

that long-range 3d antiferromagnetic order is likely to occur over the measured low temperature range. The slight leveling off of $\chi(T)$ around 5 K may be indicative of this, though small amounts of paramagnetic impurity spins can also often lead to a "Curie tail" at the lowest temperatures. The magnetization (M) versus magnetic field (H) plot also shows no magnetic hysteresis from 100 K down to 30 K, showing only a linear response with field, which also suggests the absence of long-range 3D magnetic ordering above 30 K (Figure 7d). It is interesting to compare the behavior with that of the corresponding Mn^{2+} compound $(enH_2)MnF_4$,[7] where a clear transition to a canted antiferromagnetic structure was observed just below a similar broad maximum in $\chi(T)$ that also occurred around 50 K. This suggests that, perhaps unsurprisingly, the in-plane antiferromagnetic interactions are very similar in both cases and that key differences arise due to the change in molecular species. The layer separation is significantly smaller in $(enH_2)MnF_4$[7] compared to $(pnH_2)MnF_4$, which should lead to enhanced interlayer coupling. The most likely mechanism for interlayer coupling is *via* dipolar interactions. Although $(pnH_2)MnF_4$ lacks a center of inversion between Mn^{2+} ions in adjacent layers, while $(enH_2)MnF_4$ does not (Figure 4), this seems unlikely to play a strong role due to expected the weakness of the interlayer exchange coupling.

The magnetic properties of **4** (with ∼12% antiferromagnetic CoF_2 impurities, T_N = 38.04 K)[24] have also been investigated and depicted in Figure 8. The χ versus T plot shows a trend similar to that of compound **1**. The Curie constant, C = 5.28 cm^3 mol^{-1} K and Weiss constant, θ = −132.40 K were calculated from the T > 150 K part of the $1/\chi$ versus T plot (Figure 8b), indicating an overall antiferromagnetic exchange interaction. The effective moment, μ_{eff} = 6.50 μ_B, calculated from the Curie constant, may not reflect the true value due to the impurities. Given the known and relatively low moment value of the main impurity CoF_2 (μ_{eff} = 2.210 μ_B),[25] this is unlikely to explain the high derived moment value, which as for **1** indicates a very significant orbital contribution.

The Néel temperature, T_N = 80 K, was deduced from the χT versus T plot (Figure 8c). Figure 8d shows the field dependence (−5000 to 5000 Oe) of the magnetization (M), which reveals a magnetic hysteresis at 50 K. As with **1**, the onset of spontaneous nonzero ferromagnetic moment at low field (Figure 8a), coupled with the significant hysteresis (Figure 8d), suggests that **4** is also a canted antiferromagnet. The hysteresis curve for **4** is, however, much more conventional than for **1**, with the additional linear increase with the field shown in Figure 8d typical of weak ferromagnets, as the field competes with the dominant antiferromagnetic interactions when the field is perpendicular to the ordered antiferromagnetic moments. In summary, **4** may also be regarded as a spin-canted antiferromagnet like **1.**

It is interesting to compare **3** and **4**, which are structurally similar and differ only in their transition metal species. **4** is a spin-canted antiferromagnet, while **3** is a 2D antiferromagnet, though it is not yet clear from the magnetization data whether this also later stabilizes into a 3D antiferromagnet structure. Nonetheless, the field dependence of compound **3** does not suggest any ferromagnetic component. The spin canting is most likely to rise in **4** due to DM interactions arising from the lack of an inversion center between neighboring Co^{2+} cations within the perovskite planes. The magnitude of the DM interaction is a function of orbital filling, being controlled by intersite hopping between orbitals of the same symmetry renormalized by spin orbit coupling. Changes to the balance between completely filled and partially field d orbitals lead to changes in the strength of the DM interaction (e.g., Beutier et al.[27]) For example, it was shown in ref. 26 that, in an elongated octahedral MO_6 environment, the DM coupling strength and associated spin canting angle were greatly increased for Co^{2+} compared to Mn^{2+}. In the toy tight-binding models used, this was derived mainly from the greater overlap of the higher energy orbitals. It thus seems likely that a similar explanation lies behind the very different magnetic behavior of **3** and **4**.

https://doi.org/10.1021/acs.chemmater.4c00633
Chem. Mater. XXXX, XXX, XXX−XXX

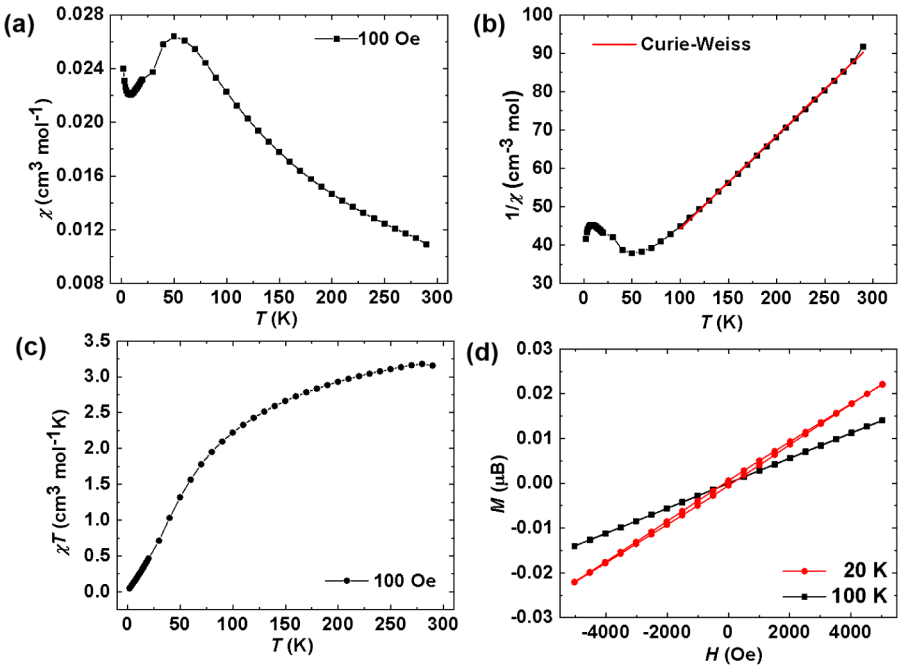

Figure 9. Magnetic data of **5**: (a) χ versus T at 100 Oe. (b) $1/\chi$ versus T and the Curie−Weiss fit to $1/\chi$ at 100 Oe. (c) χT versus T at 100 Oe. (d) Magnetization (M) versus magnetic field (H) at 20 K (red) and 100 K (black).

The magnetic properties of **5** (with ∼4.9% antiferromagnetic MnF_2 impurities) were also measured by SQUID magnetometry. Figure 9a shows the χ versus T, in which χ exhibits a broad maximum around 50 K, indicative of 2D antiferromagnetism. The observation of a Curie tail at low temperature may correspond to the presence of a small amount of paramagnetic impurities, though these cannot be identified with the main impurity MnF_2, which orders antiferromagnetically at 67.1 K. Using the $1/\chi$ versus T from $100 \leq T \leq 290$ K (Figure 9b), the Curie constant is calculated to be $C = 4.30$ cm^3 mol^{-1} K, and the Weiss constant $\theta = -83.23$ K, indicating an overall antiferromagnetic exchange interaction. The derived effective moment is $\mu_{eff} = 5.87\ \mu_B$, which is close to the spin-only value for high-spin Mn^{2+} ($5.92\ \mu_B$). Interestingly the dc χ data exhibit a feature on the low-temperature side of the broad antiferromagnetic peak, around 25 K. This position relative to the peak is a common temperature region in which to observe 3D ordering in these types of 2D antiferromagnetic materials, using techniques such as neutron powder diffraction, we might speculate that this may be the origin of this feature. However, as with sample **3**, this Mn^{2+} compound also shows no indication of canted ferromagnetism, although the low temperature field dependence does exhibit a very small hysteresis (Figure 9d). As discussed for sample **3**, **5** seems to be a 2D antiferromagnet that is likely to be long-range ordered in three dimensions at low temperatures due to dipolar interactions.

SUMMARY AND CONCLUSIONS

In all of the starting materials, the divalent metal fluoride (MF_2, M = Mn, Co, Ni) is the only source of metals. Typically, these compounds also remain as impurities in the products, even though a large excess of the diamines was applied in all the reactions (the molar masses of diamines are normally 6−8 times that of MF_2). Due to the poor solubility of MF_2 in H_2O and EG, extensive grinding before the synthesis is an effective way to reduce the remaining MF_2 impurities in the products. Apart from MF_2 impurities, the molar ratio between diamines and HF also draws our attention. Ideally, the molar quantities of HF should be twice that of the diamines in order to protonate all of the diamines in present. However, in some cases, the molar mass of HF is less. In contrast, in the synthesis of compound **7**, even though the molar mass of HF (12.5 mmol) is more than twice that of 1,4-*DAB* (6.0 mmol), the diamine has still not been protonated. That suggests all the products are the preferred outcomes for the range of synthesis conditions tested; pH has a limited effect on the formation of the products.

Among these compounds, all the perovskite layers have similar parameters (about 6 Å, which is about $2\sqrt{2}$ times the length of the M−F bond), whereas the distances between the perovskite layers are determined by the diamines (i.e., the crystallographic a-axis in **1**, **2**, **5**, and **6** and the b-axis in **3** and **4**); the diamines with longer chains will naturally build larger spacings, as long as they occur in a "stretched" conformation. In addition, the C2 and C4 series (**1**, **2**, **5**, and **6**) crystallize in the same space group, and the a-axis is correspondingly not "doubled" in these cases. In contrast, the C3 analogues (**3** and **4**) have different space groups and doubled unit cells along the layer direction. Such a difference is caused by the different octahedral tilt systems, whereby alternating layers exhibit tilts of "same sense" for even Cn (a^-a^-c) but opposite sense for odd Cn $a^-a^-c/-(a^-a^-)c$. These differences in the tilt system are themselves dictated by parity-dependent H-bonding preferences, as illustrated in Figure 4.

In each of the layered perovskites, the magnetic interactions are constructed through M−F−M bridges and form a 2D magnetic system in each perovskite octahedral layer. Due to the long distance between the perovskite layers (the shortest is 8.17 Å of $(enH_2)MF_4$) and lack of strong magnetic exchange pathways, it is not likely to form strong interplane magnetic coupling, which means that naïvely one might expect similar

https://doi.org/10.1021/acs.chemmater.4c00633
Chem. Mater. XXXX, XXX, XXX−XXX

magnetic properties for the same metal (M) regardless of the length of the diamine chain. Common characteristics include magnetic interactions that are 2D antiferromagnetic at high temperature for all samples with the cations in the high-spin states. The effective magnetic moment of the high-spin octahedral M^{2+} is much closer to the spin-only value for Mn^{2+} ($S = 5/2$, 5.92 μ_B) than for Co^{2+} ($S = 3/2$, 3.87 μ_B), since for the latter, the T_{1g} symmetry leads to an incomplete orbital quenching and hence an orbital contribution to the moment. The effective moments determined for the Co^{2+} complexes **1** and **4** are nonetheless rather high, though similar values have been seen.[28] While there is the possibility of small corrections due to the impurity phase CoF_2, it is worth noting that **1** has low levels of impurity yet yields a high effective moment, providing confidence that the high value is derived primarily from the sample. Even for **4**, the much lower moment value of the impurity CoF_2 is unlikely to lead to a significant overestimate. Similar arguments also apply to samples **3** and **5**, though the effective moments are also a little higher than the spin-only value, and it cannot be ruled out that this may in part be due to impurities. We are nonetheless confident that in all cases that the varied magnetic behavior and moment sizes measured are primarily determined by the main phase.

The octahedral rotations lead to a lack of an inversion center between neighboring M cations within the perovskite planes, allowing the possibility for anisotropic DM exchange interaction within the planes that could lead to spin canting behavior and possibly more exotic magnetic structures. Samples **3** and **4** essentially differ only in the transition metal cations, yet **4** exhibits canted antiferromagnetic behavior with a ferromagnetic component, while **3** appears to be a 2D Heisenberg antiferromagnet. This significant difference may arise due to the different fillings of the d orbitals in the Mn^{2+} and Co^{2+} materials and the consequent effect on the strength of the DM interactions. Samples **3** and **5** that both contain Mn^{2+} manifest as 2D colinear antiferromagnetic with a broad peak in the $\chi(T)$ plots around 50−60 K due to the onset of antiferromagnetic compensation. By contrast, the previously reported Mn^{2+} compound $(enH_2)MnF_4$[7] showed a clear transition to a canted antiferromagnetic structure, ordering just below a similarly broad maximum in $\chi(T)$ that also occurred around 50 K. This clear transition to long-range order is most likely precipitated by the stronger interlayer interactions in this material due to the smaller interlayer separation. Prior to ordering, the magnetic behavior of $(enH_2)MnF_4$ looks very similar to samples **3** and **5**.[7] That this also orders as a canted antiferromagnet, similar to the Co^{2+} samples **1** and **4**, does suggest an incipient tendency to do the same may be present in samples **3** and **5** due to DM interactions, albeit weaker than in the Co^{2+} samples. In the absence of other experimental indicators of long-range 3D order in samples **3** and **5**, we cannot comment further on whether these might also ultimately lead to a canted antiferromagnetic structure at a sufficiently low enough temperature.

In the absence of single crystal magnetic experiments, it is hard to comment on the likely orientation of the magnetic moment in these materials. Park et al.[29] performed anisotropic magnetization measurements on $(C_6H_5CH_2CH_2NH_3)_2MnCl_4$ (Mn-PEA) that bear some superficial similarities with the layered fluoride perovskites presented here, including the observation of canted antiferromagnetism related to DM interactions arising from the tilting of the $MnCl_4$ octahedra due to hydrogen bonding. In Mn-PEA, an easy anisotropy axis perpendicular to the perovskite layers was attributed to compression of the $MnCl_4$ octahedra, while the DM vector was suggested to lie within the plane, consistent with the observation of the observed ferromagnetic component. We can speculate about a similar interplay of single ion anisotropy and DM interactions in the materials currently presented, which exhibit analogous octahedral tilt distortions removing the inversion center at the fluoride site. Our preliminary powder neutron scattering experiments on sample **1** ($(enH_2)CoF_4$) indicate predominantly antiferromagnetic order with the moment perpendicular to the perovskite layers along a, with a small component along the in-plane c-axis. However, the magnetization data of Figure 6d suggest a potentially complex spin texture or domain structure that might prove difficult to deduce from powder diffraction alone.

In summary, we have prepared and extended the examples of layered hybrid fluoride perovskites, some of which show evidence for net switchable magnetization at low temperature, which could have potential applications as magnetic materials. Further work is necessary to prepare phase-pure samples or large single crystals for more detailed magnetic characterization, including neutron diffraction studies of the magnetic ordering. The unexpected layered structure of **7** is also very interesting, and preparation of a phase-pure sample to study its magnetic properties should also be a target for further studies.

■ ASSOCIATED CONTENT

Supporting Information

The Supporting Information is available free of charge at https://pubs.acs.org/doi/10.1021/acs.chemmater.4c00633.

Synthetic details, supplementary crystallographic data and powder diffraction data; Rietveld plot (PXRD, $CuK_{\alpha 1}$) for **1** (Figure S1), for **2**. (Figure S2), for **3** (Figure S3), for **4** (Figure S4), for **5** (Figure S5); for **6** (Figure S6), and for **7** (Figure S7); selected BLs and bond valences (Tables S1 and S2) (PDF)

Accession Codes

ccdc 2259787−2259799 contain the supplementary crystallographic data for this paper. These data can be obtained free of charge via www.ccdc.cam.ac.uk/data_request/cif, or by emailing data_request@ccdc.cam.ac.uk, or by contacting The Cambridge Crystallographic Data Centre (CCDC), 12 Union Road, Cambridge CB2 1EZ, UK; fax: + 44 1223 336033.

■ AUTHOR INFORMATION

Corresponding Author

Philip Lightfoot − *School of Chemistry and EaStChem, University of St Andrews, St Andrews KY16 9ST, United Kingdom;* orcid.org/0000-0001-7048-3982; Email: pl@st-andrews.ac.uk

Authors

Teng Li − *School of Materials and Energy, University of Electronic Science and Technology of China, Chengdu 611731, China;* orcid.org/0000-0003-4238-3284

Alasdair J. Bradford − *School of Chemistry and EaStChem, University of St Andrews, St Andrews KY16 9ST, United Kingdom*

Stephen L. Lee − *School of Physics and Astronomy, University of St Andrews, St Andrews KY16 9SS, United Kingdom*

https://doi.org/10.1021/acs.chemmater.4c00633
Chem. Mater. XXXX, XXX, XXX−XXX

Complete contact information is available at:
https://pubs.acs.org/10.1021/acs.chemmater.4c00633

Notes

The authors declare no competing financial interest.

■ ACKNOWLEDGMENTS

We acknowledge support from the University of St Andrews, the China Scholarship Council (201606280032, PhD studentship to TL), and the China Postdoctoral Science Foundation (2022M710619).

■ REFERENCES

(1) Adil, K.; Leblanc, M.; Maisonneuve, V.; Lightfoot, P. Structural chemistry of organically-templated metal fluorides. *Dalton Trans.* **2010**, *39*, 5983−5993.
(2) Francis, R. J.; Halasyamani, P. S.; O'Hare, D. The first organically-templated layered uranium(IV) fluorides $(H_3N(CH_2)_3)NH_3)U_2F_{10}.2H_2O$, $(H_3N(CH_2)_4)NH_3)U_2F_{10}.3H_2O$ and $(H_3N(CH_2)_6)NH_3)U_2F_{10}.2H_2O$. *Angew. Chem.* **1998**, *37*, 2214−2217.
(3) Bentrup, U.; Feist, M.; Kemnitz, E. Halogenometalates with N-containing organic cations: structural chemistry and thermal behaviour. *Prog. Solid State Chem.* **1999**, *27*, 75−129.
(4) Smith, M. D.; Crace, E. J.; Jaffe, A.; Karunadasa, H. I. The Diversity of Layered Halide Perovskites. *Annu. Rev. Mater. Res.* **2018**, *48*, 111−136.
(5) Li, X.; Hoffman, J. D.; Kanatzidis, M. D. The 2D Halide Perovskite Rulebook: How the Spacer Influences Everything from the Structure to Optoelectronic Device Efficiency. *Chem. Rev.* **2021**, *121* (4), 2230−2291.
(6) McNulty, J. A.; Lightfoot, P. Structural chemistry of layered lead halide perovskites containing single octahedral layer. *IucrJ* **2021**, *8*, 485−513.
(7) Li, T.; Clulow, R.; Bradford, A. J.; Lee, S. L.; Slawin, A. M. Z.; Lightfoot, P. A hybrid fluoride layered perovskite, $(enH_2)MnF_4$. *Dalton Trans.* **2019**, *48*, 4784−4787.
(8) Li, C.; Lu, X.; Ding, W.; Feng, L.; Gao, Y. H.; Guo, Z. Formability of ABX_3 (X = F, Cl, Br, I) halide perovskites. *Acta Crystallogr. B* **2008**, *64*, 702−707.
(9) Travis, W.; Glover, E. N. K.; Bronstein, H.; Scanlon, D. O.; Palgrave, R. G. On the application of the tolerance factor to inorganic and hybrid halide perovskites: a revised system. *Chem. Sci.* **2016**, *7*, 4548−4556.
(10) Shannon, R. D. Revised Effective Ionic Radii and Systematic Studies of Interatomic Distances in Halides and Chalcogenides. *Acta Crystallogr.* **1976**, *A32*, 751−767.
(11) Leblanc, M.; Maisonneuve, V.; Tressaud, A. Crystal Chemistry and Selected Physical Properties of Inorganic Fluorides and Oxide-Fluorides. *Chem. Rev.* **2015**, *115*, 1191−1254.
(12) Li, T.; Lightfoot, P. Layered hybrid iron fluorides. *Crystals* **2022**, *12*, 1443.
(13) Balachandran, P. V.; Young, J.; Lookman, T.; Rondinelli, J. M. Learning from data to design functional materials without inversion symmetry. *Nat. Commun.* **2017**, *8*, 14282.
(14) Xu, W.-J.; Kopyl, S.; Kholkin, A.; Rocha, J. Hybrid organic-inorganic perovskites: Polar properties and applications. *Coord. Chem. Rev.* **2019**, *387*, 398−414.
(15) Rigaku. *CrystalClear*; Rigaku Corporation: Tokyo, Japan, 2015.
(16) Sheldrick, G. M. *SHELXL-2018, Program for the Refinement of Crystal Structures*; University of Göttingen: Göttingen, Germany, 2018.
(17) Farrugia, L. J. WinGX and ORTEP for Windows: an update. *J. Appl. Crystallogr.* **2012**, *45*, 849−854.
(18) Toby, B. H. EXPGUI, a graphical user interface for GSAS. *J. Appl. Crystallogr* **2001**, *34*, 210−213.
(19) Kind, R.; Plesko, S.; Günter, P.; Roos, J.; Fousek, J. Structural phase transitions in the perovskite-type layer compounds $NH_3(CH_2)_3NH_3CdCl_4$, $NH_3(CH_2)_4NH_3MnCl_4$, and $NH_3(CH_2)_5NH_3CdCl_4$. *Phys. Rev. B* **1981**, *23*, 5301−5315.
(20) Han, C.; Bradford, A. J.; Slawin, A. M. Z.; Bode, B. E.; Fusco, E.; Lee, S. L.; Tang, C. C.; Lightfoot, P. Structural Features in Some Layered Hybrid Copper Chloride Perovskites: $ACuCl_4$ or A_2CuCl_4. *Inorg. Chem.* **2021**, *60*, 11014−11024.
(21) Aleksandrov, K. S.; Bartolomé, J. Structural distortions in families of perovskite-like crystals. *Phase Transitions* **2001**, *74* (3), 255−335.
(22) Strempfer, J.; Rutt, U.; Bayrakci, S. P.; Bruckel, T.; Jauch, W. Magnetic properties of transition metal fluorides MF_2 (M = MN, Fe, Co, Ni) via high-energy photon diffraction. *Phys. Rev. B* **2004**, *69*, 014417.
(23) Hoffmann, A.; Sort, J.; Buchanan, K. S.; Nogués, J. Exchange-biased magnetic vortices. *IEEE Trans. Magn.* **2008**, *44*, 1968−1973.
(24) Turberfield, K. C.; Okazaki, A.; Stevenson, R. W. H. The development of the magnetic excitation spectra of MnF_2 with increasing temperature. *Proc. Phys. Soc.* **1965**, *85*, 743−758.
(25) Jauch, W.; Reehuis, M.; Schultz, A. J. γ-ray and neutron diffraction studies of CoF_2: magnetostriction, electron density and magnetic moments. *Acta Crystallogr. A* **2004**, *60*, 51−57.
(26) Cowley, R. S.; Carneiro, K. Critical properties of pure and random antiferromagnets: CoF_2, Co/ZnF_2 and KMn/NiF_3. *J. Phys. C: solid State Phys.* **1980**, *13*, 3281−3291.
(27) Beutier, G. Band-filling control of the Dzyaloshinskii-Moriya interaction in weakly ferromagnetic insulators. *Phys. Rev. Lett.* **2017**, *119*, 167201.
(28) Ishikawa, H.; Imajo, S.; Takeda, H.; Kakegawa, M.; Yamashita, M.; Yamaura, J.; Kindo, K. J_{eff}= 1/2 hyperoctagon lattice in cobalt oxalate metal-organic framework. *Phys. Rev. Lett.* **2024**, *132*, 156702.
(29) Park, S.-H.; Oh, I.-H.; Park, S.; Park, Y.; Kim, J. H.; Huh, Y.-D. Canted antiferromagnetism and spin reorientation transition in layered inorganic-organic perovskite $(C_6H_5CH_2CH_2NH_3)_2MnCl_4$. *Dalton Trans.* **2012**, *41*, 1237−1242.